

Multi-energy reconstructions, central electron temperature measurements, and early detection of the birth and growth of runaway electrons using a versatile soft x-ray pinhole camera at MST

Cite as: Rev. Sci. Instrum. **92**, 073502 (2021); <https://doi.org/10.1063/5.0043672>

Submitted: 10 January 2021 . Accepted: 26 April 2021 . Published Online: 02 July 2021

 L. F. Delgado-Aparicio,  P. VanMeter,  T. Barbui,  O. Chellai,  J. Wallace, H. Yamazaki,  S. Kojima, A. F. Almagari,  N. C. Hurst,  B. E. Chapman, K. J. McCollam, D. J. Den Hartog, J. S. Sarff, L. M. Reusch,  N. Pablant,  K. Hill, M. Bitter,  M. Ono, B. Stratton,  Y. Takase, B. Luethi,  M. Rissi,  T. Donath, P. Hofer, and  N. Pilet

COLLECTIONS

Paper published as part of the special topic on [Proceedings of the 23rd Topical Conference on High-Temperature Plasma Diagnostics](#)



[View Online](#)



[Export Citation](#)



[CrossMark](#)

ARTICLES YOU MAY BE INTERESTED IN

[Entangled photon-pair sources based on three-wave mixing in bulk crystals](#)

Review of Scientific Instruments **92**, 041101 (2021); <https://doi.org/10.1063/5.0023103>

[Correction and verification of x-ray imaging crystal spectrometer analysis on Wendelstein 7-X through x-ray ray tracing](#)

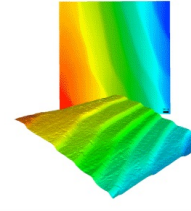
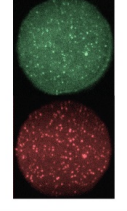
Review of Scientific Instruments **92**, 043530 (2021); <https://doi.org/10.1063/5.0043513>

[Characterizing materials for superconducting radiofrequency applications—A comprehensive overview of the quadrupole resonator design and measurement capabilities](#)

Review of Scientific Instruments **92**, 064710 (2021); <https://doi.org/10.1063/5.0046971>

Review of Scientific Instruments

AIP
Publishing

| | | | | |
|---|--|---|---|--|
|  MAD CITY LABS INC. www.madcitylabs.com | Nanopositioning Systems  | Modular Motion Control  | AFM and NSOM Instruments  | Single Molecule Microscopes  |
|---|--|---|---|--|

Multi-energy reconstructions, central electron temperature measurements, and early detection of the birth and growth of runaway electrons using a versatile soft x-ray pinhole camera at MST

Cite as: Rev. Sci. Instrum. 92, 073502 (2021); doi: 10.1063/5.0043672

Submitted: 10 January 2021 • Accepted: 26 April 2021 •

Published Online: 2 July 2021



View Online



Export Citation



CrossMark

L. F. Delgado-Aparicio,^{1,a)} P. VanMeter,² T. Barbui,¹ O. Chellai,¹ J. Wallace,² H. Yamazaki,³ S. Kojima,⁴ A. F. Almagari,² N. C. Hurst,² B. E. Chapman,² K. J. McCollam,² D. J. Den Hartog,² J. S. Sarff,² L. M. Reusch,⁵ N. Pablant,¹ K. Hill,¹ M. Bitter,¹ M. Ono,¹ B. Stratton,¹ Y. Takase,⁶ B. Luethi,⁷ M. Rissi,⁷ T. Donath,⁷ P. Hofer,⁷ and N. Pilet⁷

AFFILIATIONS

¹ Princeton Plasma Physics Laboratory, Princeton, New Jersey 08540, USA

² University of Wisconsin-Madison, Madison, Wisconsin 53706, USA

³ National Institutes for Quantum and Radiological Science and Technology, Naka, Ibaraki 311-0193, Japan

⁴Kyushu University, Kasuga-kouen 6-1, Kasuga, Japan

⁵Edgewood College, Madison, Wisconsin 53711, USA

⁶The University of Tokyo, Kashiwa 277-8561, Japan

⁷DECTRIS Ltd., 5405 Baden-Dättwil, Switzerland

Note: Paper published as part of the Special Topic on Proceedings of the 23rd Topical Conference on High-Temperature Plasma Diagnostics.

a)Author to whom correspondence should be addressed: ldelgado@pppl.gov

ABSTRACT

A multi-energy soft x-ray pinhole camera has been designed, built, and deployed at the Madison Symmetric Torus to aid the study of particle and thermal transport, as well as MHD stability physics. This novel imaging diagnostic technique employs a pixelated x-ray detector in which the lower energy threshold for photon detection can be adjusted independently on each pixel. The detector of choice is a PILATUS3 100 K with a 450 μm thick silicon sensor and nearly 100 000 pixels sensitive to photon energies between 1.6 and 30 keV. An ensemble of cubic spline smoothing functions has been applied to the line-integrated data for each time-frame and energy-range, obtaining a reduced standard-deviation when compared to that dominated by photon-noise. The multi-energy local emissivity profiles are obtained from a 1D matrix-based Abel-inversion procedure. Central values of T_e can be obtained by modeling the slope of the continuum radiation from ratios of the inverted radial emissivity profiles over multiple energy ranges with no *a priori* assumptions of plasma profiles, magnetic field reconstruction constraints, high-density limitations, or need of shot-to-shot reproducibility. In tokamak plasmas, a novel application has recently been tested for early detection, 1D imaging, and study of the birth, exponential growth, and saturation of runaway electrons at energies comparable to $100 \times T_{e,0}$; thus, early results are also presented.

Published under license by AIP Publishing. <https://doi.org/10.1063/5.0043672>

I. INTRODUCTION AND MOTIVATION

One of the main challenges of conventional x-ray tomographic diagnostics is the inference of basic plasma parameters (e.g., T_e ,

$n_{e,Z}$, and Z_{eff}) from magnetically confined fusion plasmas; this limitation stems from their inability to sample the local photon energy-distribution since these systems are fielded with standard filtered-diode arrays measuring the space- and energy-integrated

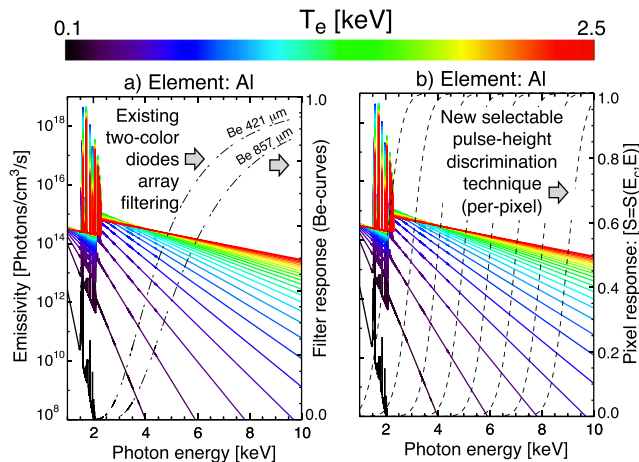


FIG. 1. FLYCHK¹¹ x-ray spectra for Al at multiple values of electron temperatures between 0.1 and 2.5 keV. The dotted lines in (a) correspond to the transmission of the thick Be-filters while those in (b) correspond to the pixel responsivity curves for the ME-SXR system between 2 and 9 keV.

x-ray power. The novel multi-energy soft x-ray (ME-SXR) pin-hole camera diagnostic presented in this paper removes these limitations and is capable of measuring the time-history of the local x-ray emissivity in multiple energy ranges simultaneously, from which it is possible to infer profiles of core measurements of electron temperature (T_e) and impurity density (n_Z) with no *a priori* assumptions of plasma profiles, magnetic field reconstruction constraints, high-density limitations, or need of shot-to-shot reproducibility. Analysis can be complicated by the presence of bright He- and H-like metal emission lines, but adequate energy discrimination at a pixel-level can circumvent these difficulties.

A first proof-of-principle diagnostic system based on a PILATUS² detector was deployed at the Alcator C-Mod tokamak at MIT in 2012 with good results.² A collaboration between PPPL and the Physics Department at the University of Wisconsin–Madison was established to design, build, install, and operate an ME-SXR pinhole camera based on the newer PILATUS³ technology at the Madison Symmetric Torus (MST).^{3,4} The initial benefit to the MST program lies in the ability of the new detector to characterize the Al line-radiation present in the MST, which nicely complements the data obtained with the existent two-color diode array suite, which uses conventional Be filters with 50% transmission at 4 and 5 keV⁶ (see Fig. 1). The strong emission from the Al recombination edges as well as line-radiation from He-like and H-like charge states—commonly found at temperatures from 0.5 to 1–2 keV—has been a persistent challenge in the interpretation of the MST’s x-ray data for many years.^{6–10}

II. ENERGY RESOLUTION AND CHARGE SHARING

The compact vacuum-compatible system shown in Figs. 2(a) and 2(b) monitors the radial time history profiles of the medium-Z emission at multiple energy ranges in all MST RFP scenarios. The detector allowed us to set pixels at different energy ranges according to characteristic cutoff-energies (E_c) or thresholds, with response widths of ~ 0.35 keV. The new configuration of pixelated

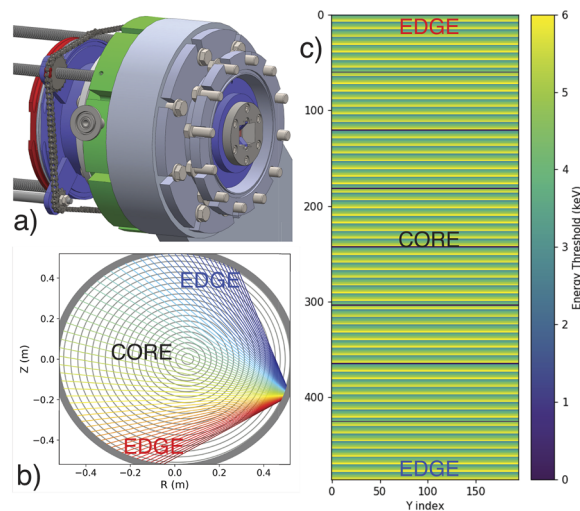


FIG. 2. (a) Compact view of ME-SXR at the MST imaging most of its (b) circular cross section. (c) The cutoff energy for the 2D system was arranged constant in rows from 2 to 5.5 keV in repeating groups for a total of 60 chords each.

detectors is shown in Fig. 2(c). Here, an entire row of pixels would be effectively used for each energy value since by skipping pixel rows, only redundant spatial information would be discarded. It is, therefore, possible to obtain coarse spectral resolution by setting the pixels in each row to varying energy thresholds, E_1, E_2, \dots, E_8 , etc (from 2 to 5.5 keV in coarse steps of 0.5 keV). The configurations of pixelated detectors can be further optimized based on the Shannon–Nyquist¹² sampling and interpolation theory since the observed spectra are typically oversampled. The detector electronic response (S -curves, equivalent to a filter transmission function) shown in Figs. 1(b) and 3 can be described by a functional form,

$$S(E, E_c, \sigma_E) = \frac{1}{2} \operatorname{erfc}\left(-\frac{E - E_c}{\sqrt{2}\sigma_E}\right), \quad (1)$$

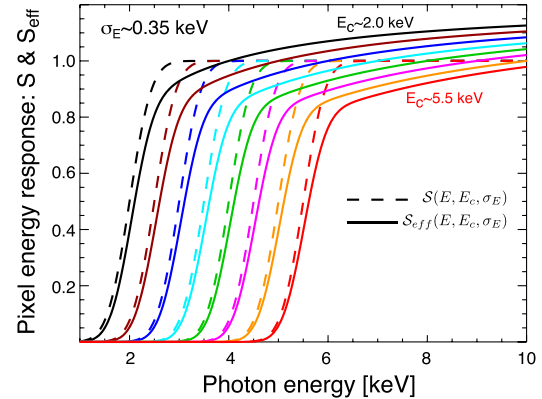


FIG. 3. Ideal and effective (with charge-sharing effects) detector electronic response S -curves used in the low-energy configuration for E_c ’s between 2 and 5.5 keV.

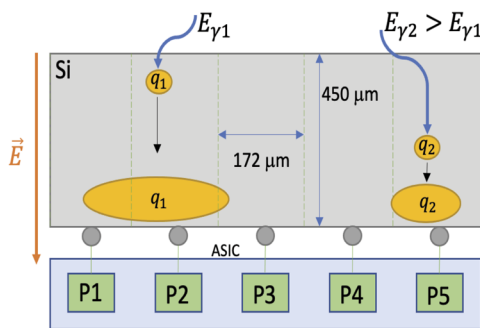


FIG. 4. Simplified cartoon illustrating the basic concepts of charge-sharing due to Coulomb repulsion.

where E_c is the 50% cutoff energy and σ_E is the energy resolution of the order of 0.35 keV.^{9,13,14} The ability to set an energy threshold at an arbitrary value with constant energy resolution is a significant improvement over metallic foil systems.^{15–17} The resultant spatial resolution of the present design is of the order of 1 cm, and the maximum frame rate of the PILATUS3 system is 500 Hz.

Charge sharing is a common phenomenon in all types of 2D detectors, which rely on a monolithic absorbing material to convert photons to photo-electrons before transporting electric charges to the application-specific integrated circuit (ASIC). This process is illustrated schematically in Fig. 4. As the charge generated by x-rays drifts toward discrete detector elements, the electron cloud will expand due to its own Coulomb repulsion. As a result, a fraction of the “cloud charge” may be collected by an adjacent pixel, thereby appearing to be two photons of lower energy in comparison to the

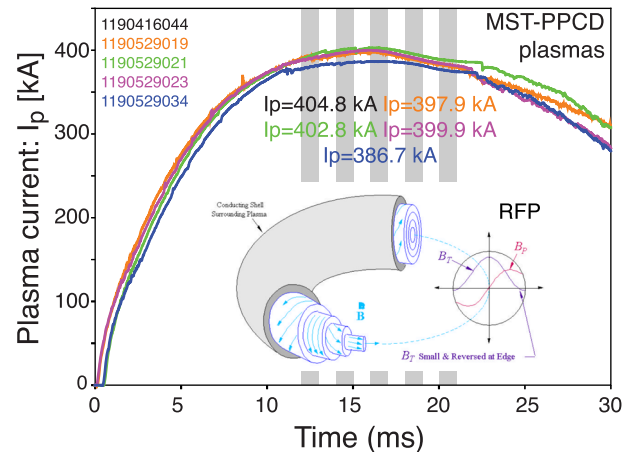


FIG. 5. I_p traces during 400 kA RFP plasmas at the MST. Vertical columns indicate the 1 ms integration windows during the high-confinement PPCD scenarios.

original. This effect is important for low-energy incoming photons as they will produce photo-electrons in the “top” layers of the silicon-lattice in comparison to more energetic photons, which will produce the effective charge deeper in the lattice and closer to the bump-ons and the ASIC.

Since the pixels can be arranged to have different threshold energies, it is prudent to characterize this effect and incorporate it in a diagnostic forward model. The key insight developed by Kraft^{18,19} suggests that the impact of charge sharing [see the sketch in Fig. 4(b)] is determined by the ratio of the area surrounding the pixel border—for which charge-sharing is significant—to the total

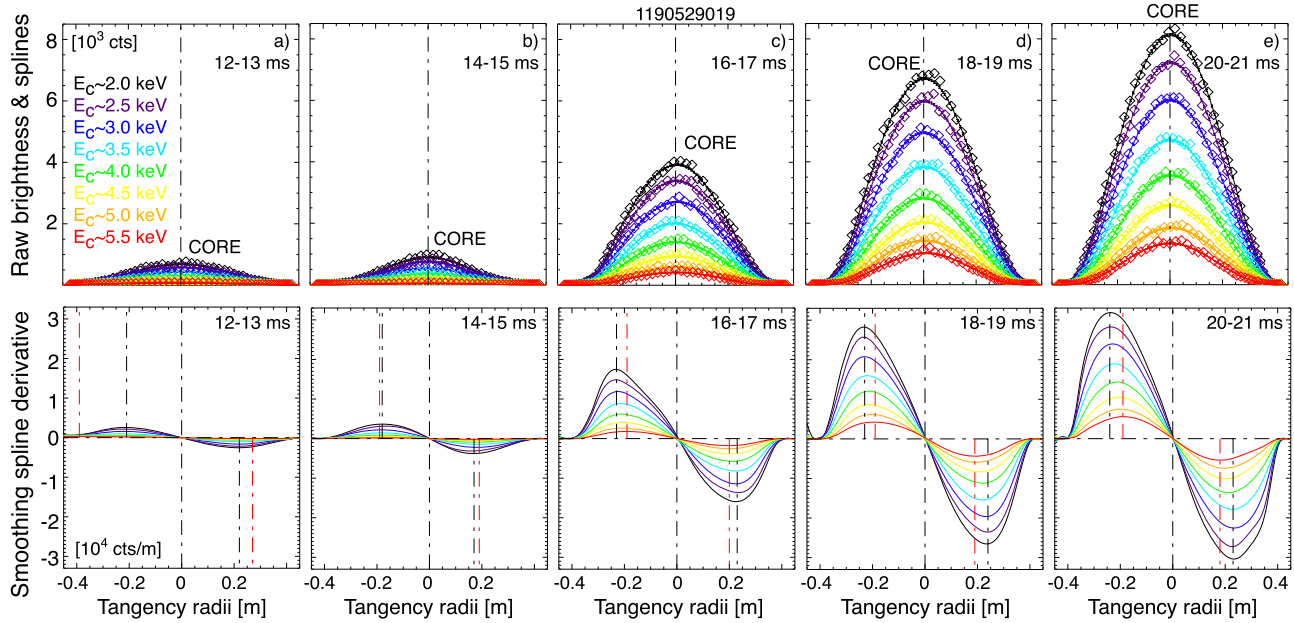


FIG. 6. Time-history of multi-energy raw brightness-data, smoothing splines, and spatial derivatives ready for reconstruction for the times indicated in Fig. 5 and cutoff energies of 2.0, 2.5, 3.0, 3.5, 4.0, 4.5, 5.0, and 5.5 keV.

pixel area such that $f \equiv A_{CS}/A_{pixel} = -kE/2$. Since this effect is based on the physical drift of electrons in the detector, the charge-sharing slope is independent of the detector gain setup at the ASIC level. For the detector installed at the MST, $f = 0.266 \pm 0.008$, and is in good agreement with the study by Kraft.^{18,19} Charge sharing then leads to a linear distortion in the observed counts for a given energy E as the threshold energy (E_c) is varied. This is a straightforward effect leading to an effective $\mathcal{S}_{eff} = \mathcal{S} \cdot \mathcal{F}$ where

$$\mathcal{F}(E, E_c) = \frac{1 + 2f \cdot (1 - E_c/E)}{1 + f}. \quad (2)$$

III. BRIGHTNESS AND EMISSIVITY PROFILES

The first tests were conducted using a detector setting with an eight-color configuration and a 60-chord (per color) detector imaging a fusion grade high-confinement Pulse Poloidal Current Drive (PPCD) plasma.^{4,5} Time history traces are depicted in Fig. 5, showing the five time-points characteristic of the transition to PPCD; in short, the edge current drive increases $J_{||}$, which decreases the current gradient, thus suppressing tearing modes and leading to the transient low-density ($n_{e,0} \sim 10^{19} \text{ m}^{-3}$) but high-temperature ($T_{e,0} \sim 1 \text{ keV}$) high-confinement regime.

The raw ME line-integrated brightness for the five time-points and eight energy ranges is shown in Fig. 6. The smoothing and inversion procedure is as follows: First, a cubic spline smoothing procedure was used to process the line-integrated data using a smoothing parameter calculated from the “rms” noise of the signal. The derivative also provides a measurement of the plasma centroid and a figure of merit for the presence of asymmetries. If the x-ray emission from toroidal axisymmetric plasmas has circular symmetry, it can be computed using the standard 1D-Abel equation through a simple “pre-calculated” matrix-based²⁰ operation, as shown in Fig. 7.

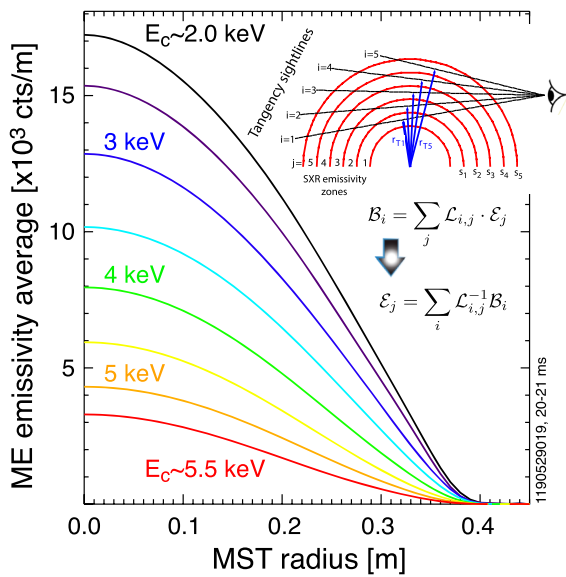


FIG. 7. Average emissivities reconstructed simultaneously for the time-point shown in Fig. 6(e) and for cutoff energies between 2.0 and 5.5 keV. The insets show the benefits of using a matrix-based Abel-reconstruction routine.

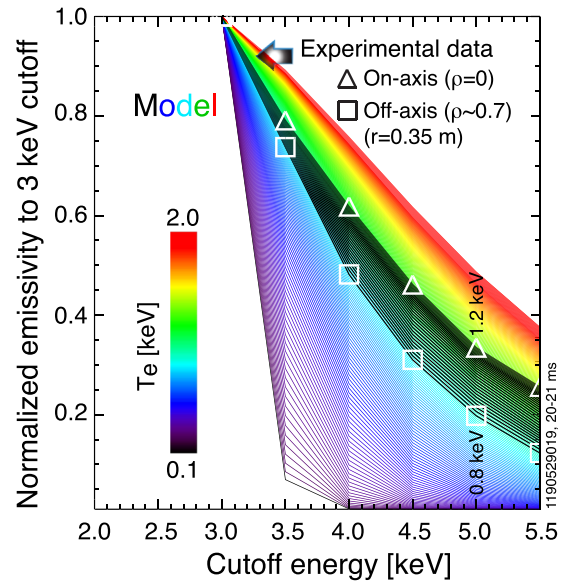


FIG. 8. Energy dependence of normalized emissivities for on-axis and off-axis radii; the experimental data have been superimposed to that of a model that include all elements in the diagnostic chain including charge-sharing.

The photon-energy dependence of the normalized emissivities with respect to that with $E_c = 3.0 \text{ keV}$ is shown in Fig. 8; this normalization choice is due to the possible line-pollution from He- and H-like Al emission lines shown in Fig. 1. The experimental data have been superimposed to that of the model that includes the plasma continuum emission and all elements in the diagnostic chain such as transmission through Be, Mylar, absorption in Si, and the typical responsivity curve [Eq. (1)] including charge-sharing [Eq. (2)]. The typical $\exp(-E_c/T_e)$ energy-dependence suggests that T_e on-axis is of the order of $\sim 1.2 \text{ keV}$, while it is $\sim 0.8 \text{ keV}$ at $r/a \sim 0.7$ (or $r = 0.35 \text{ m}$ for $a = 0.5 \text{ m}$). The profile measurement will be a subject of a future contribution.

IV. DETECTION OF RUNAWAY ELECTRONS IN LOW TOKAMAK SCENARIOS AT THE MST

Runaway electrons (REs) and disruptions are two of the “Achilles heels” for tokamak devices. The toroidal electric fields generated during the low-density plasma current quench can accelerate electrons well above their thermal speed, leading to an exponential growth and saturation of a highly-energetic runaway population, which can cause significant damage to the plasma-facing components (PFCs). The majority of steady-state RE studies have been conducted in tokamak plasmas with “keV” electron temperatures and electron energies up to 2–30 MeV,^{21,22} and thus, the ratio of photon energy to temperature is nearly $E_{x,y}/T_{e,0} \sim 1000\text{--}30\,000$.

REs are now also generated at the MST²³ in steady tokamak scenarios with low current and toroidal magnetic field obtaining plasmas with core temperatures and densities of the order of 0.1 keV and $< 0.1 \times 10^{19} \text{ m}^{-3}$, respectively. Density thresholds for both runaway electron onset and suppression are determined with simple variations in gas puffing, and the presence of runaways is usually detected

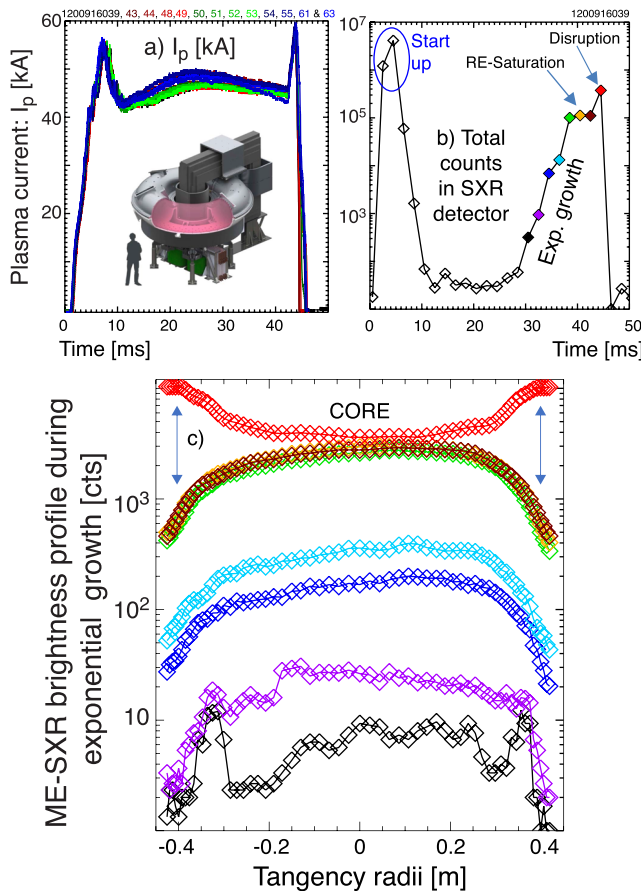


FIG. 9. (a) Tokamak I_p traces for reproducible discharges. The time-history of the total number of counts on the detector during a typical “shot” is depicted in (b) while the time evolution of the spatially resolved profiles during the RE exponential growth and disruption is shown in (c).

via emission of non-thermal x-ray photons and using a fast single-diode measurement.²³ The use of the novel silicon ME-SXR pin-hole camera allows for a significant improvement for early detection, 1D imaging, and energy discrimination of REs at $E_{x,y}/T_{e,0} \sim 50\text{--}500$.

Reproducible tokamak discharges with $I_p = 40\text{--}50$ kA and $B_{\phi,wall} = 1.4$ kG are routinely obtained, as shown in Fig. 9(a). For these initial experiments, the entire detector was operated at a cutoff-energy of 2 keV to increase the signal-to-noise ratio (SNR) ratio at these low-densities; the low-temperature thermal background plasma has negligible x-rays: > 2 keV. The time-history of the total count in the SXR detector depicted in Fig. 9(b) shows non-thermal maxima at the start ($t \sim 5$ ms) where “hard” x-rays are expected due to the high-electric field needed for the ionization. As the ramp-up electric field decreases, the fast electrons vanish quickly. The pre-programmed density ramp-down ($\langle n_e \rangle = 0.16 \rightarrow 0.05 \times 10^{19} \text{ m}^{-3}$ from 18 to 33 ms) generates fast-electrons as the Dreicer field scales proportional with density. The exponential growth of the signal shown in Fig. 9(b) suggests that runaway electrons form from $t = 25$ to 40 ms, reaching saturation and a sudden

disruption. In addition, the 1D brightness profile shown in Fig. 9(c) has interesting features, changing from hollow to peaked to hollow again before the disruption, a process which is currently under investigation.

V. SUMMARY

A compact ME-SXR pinhole camera has been in operation at the MST-device to fully exploit the novel diagnostic capability for magnetically confined fusion plasmas as well as aid the study of particle and thermal-transport and MHD stability physics. Central values of electron temperature have been measured up to ~1.2 keV during RFP plasmas; during low-density tokamak scenarios, this camera has also assisted in the early detection, imaging, and study of the birth, exponential growth, and saturation of runaway electrons at energies $100 \times T_{e,0}$.

ACKNOWLEDGMENTS

This work was supported by the U.S. DOE-OFES, under Contract No. DE-AC02-09CH11466, and LFDA’s 2015 DOE Early Career Award Research Program. The experiments were conducted at the Wisconsin Plasma Physics Laboratory (WiPPL), a research facility supported by the DOE-OFES, under Contract No. DE-SC0018266, with major facility instrumentation developed with the support from the NSF, under Award No. PHY 0923258. The MST Tokamak Thermal Quench Program is funded under DOE-OFES, Award No. DE-SC0020245.

DATA AVAILABILITY

The data that support the findings of this study are available from the corresponding author upon reasonable request.

REFERENCES

- See <https://www.dectris.com> for information of SXR and HXR detectors.
- L. F. Delgado-Aparicio *et al.*, *Rev. Sci. Instrum.* **87**, 11E204 (2016).
- R. N. Dexter *et al.*, *Fusion Technol.* **19**, 131 (1991).
- J. S. Sarff *et al.*, *Phys. Rev. Lett.* **72**, 3670 (1994).
- B. E. Chapman *et al.*, *Phys. Rev. Lett.* **87**, 205001 (2001).
- L. M. Reusch *et al.*, *Rev. Sci. Instrum.* **85**, 11D844 (2014).
- M. E. Galante *et al.*, *Nucl. Fusion* **55**, 123016 (2016).
- H. Yamazaki *et al.*, *Rev. Sci. Instrum.* **89**, 10G120 (2018).
- P. van Meter *et al.*, *Rev. Sci. Instrum.* **89**, 10G119 (2018).
- L. F. Delgado-Aparicio *et al.*, *Rev. Sci. Instrum.* **89**, 10G116 (2018).
- H.-K. Chung *et al.*, *High Energy Density Phys.* **1**, 3 (2005).
- E. Wang *et al.*, *Rev. Sci. Instrum.* **83**, 10E139 (2012).
- N. A. Pablant *et al.*, *Rev. Sci. Instrum.* **83**, 10E526 (2012).
- J. Maddox *et al.*, *Rev. Sci. Instrum.* **87**, 11E320 (2016).
- L. F. Delgado-Aparicio *et al.*, *Plasma Phys. Controlled Fusion* **49**, 1245 (2007).
- L. Delgado-Aparicio *et al.*, *Rev. Sci. Instrum.* **81**, 10E303 (2010).
- L. Delgado-Aparicio *et al.*, PPPL-Report No. 4977, 2014.
- P. Kraft *et al.*, *IEEE Trans. Nucl. Sci.* **56**, 758 (2009).
- P. Kraft *et al.*, *J. Synchrotron Radiat.* **16**, 368 (2009).
- R. E. Bell, *Rev. Sci. Instrum.* **66**, 558 (1995).
- C. Paz-Soldan *et al.*, *Phys. Plasmas* **21**, 022514 (2014).
- C. Paz-Soldan *et al.*, *Phys. Plasmas* **25**, 056105 (2014).
- S. Munaretto *et al.*, *Nucl. Fusion* **60**, 046024 (2020).